Computed-tomography imaging spectrometer: experimental calibration and reconstruction results

Michael Descour and Eustace Dereniak

A temporally and spatially nonscanning imaging spectrometer is described in terms of computed-tomography concepts, specifically the central-slice theorem. A sequence of three transmission sinusoidal-phase gratings rotated in 60° increments achieves dispersion in multiple directions and into multiple orders. The dispersed images of the system's field stop are interpreted as two-dimensional projections of a three-dimensional (x, y, λ) object cube. Because of the size of the finite focal-plane array, this imaging spectrometer is an example of a limited-view-angle tomographic system. The imaging spectrometer's point spread function is measured experimentally as a function of wavelength and position in the field of view. Reconstruction of the object cube is then achieved through the maximum-likelihood, expectation-maximization algorithm under the assumption of a Poisson likelihood law. Experimental results indicate that the instrument performs well in the case of broadband and narrow-band emitters.

Key words: Imaging spectrometry, computed tomography, experimental point-spread-function characterization, central-slice theorem, missing cones.

1. Introduction

The objective of imaging spectrometry is the acquisition of a set of registered, spectrally contiguous images of a scene's spatial-radiance distribution. This objective is an extension of that of classical imaging systems that acquire broadband images. The availability of a spectrum at each picture element (pixel) provides additional insight into the nature of a scene. Spectral data can reveal the condition or identity of object–space elements in vegetation monitoring,[1] mineral identification,[1] detection of chemical agents, temperature and emissivity estimation, and medical-imaging applications.

The emergence of two critical technologies is offering new opportunities in hyperspectral-imaging applications. The first technological development is the staring focal-plane array (FPA), available in increasingly large formats (e.g., 62 mm × 62 mm, 26.2 million pixels[2]) and spectral responsivities that cover the visible (400–800-nm) and IR (3–5- and 8–12-µm) parts of the spectrum. The second critical development is computing technology, which makes computationally intensive, indirect forms of imaging a reality. We propose achieving the objective of imaging spectrometry without scanning by taking full advantage of large FPA's and fast computers. Furthermore the imaging-spectrometry approach presented in this paper has the potential for enhanced performance resulting from advancements in those two technologies.

2. Object Cube

An imaging spectrometer acquires a three-dimensional (3D) data set. Two of the set's dimensions are spatial (x and y), whereas the third is spectral (wavelength λ). The spatial coordinates refer to an image plane within the optical system at which the field of view is defined. This 3D data set is sometimes called a data cube, but we christen it an object cube to avoid confusion with upcoming nomenclature.

Figure 1 shows the manner in which several conventional spectrometers acquire data about the object cube. A spectrometer utilizing a grating and a linear array of detectors provides data about a column, a, within the object cube. The output of a spectrally filtered staring camera is a plate, b, whose thickness $\Delta\lambda$ is determined by a filter's bandpass. A slit spectrometer using a dispersive element and a two-dimensional (2D) FPA performs one-dimensional spec-
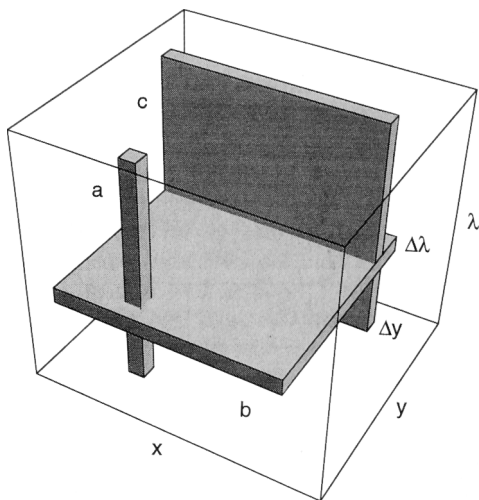
Fig. 1.   Object cube and data-acquisition modes characteristic of several conventional spectrometer types.

Fig. 2.   Nonscanning imaging spectrometer layout.   The upper half of the diagram is a cutaway view of the system optics.

tral imaging and produces information describing a plate of a finite width Δy, c.   Width Δy governs the spectral resolution and together with the slit's length determines the instantaneous field of view.   The feature common to all these instruments is the need to scan in space or along the spectral dimension to measure the entire object cube.

Scanning is also required by multiplexing spectrometers.   In a Fourier-transform spectrometer (FTS) and a Hadamard-transform spectrometer, a detector integrates a weighted sum of emissions from multiple spectral bands.   In the case of the FTS the weights are determined by the spectral amplitude as well as the spectral-interferogram phase at the detector. In the case of the Hadamard-transform instrument[3] the weights are unity or zero and determined by a set of masks that block certain spectral bands and transmit others.   Spectral imaging in all cases discussed thus far requires the configuration of the instrument to change.   For example, mirrors must be moved or a different filter must be rotated into the optical train.

The elimination of scanning is motivated by two factors.   First, the configuration of the imaging spectrometer becomes fixed.   The absence of moving parts results in a rugged design well suited to hazardous and demanding environments.   Second, the instantaneous collection of all data needed for the spatial and spectral description of object space means that dynamic events within the field of view can be spectrally imaged.

In computed-tomography imaging spectrometry, a detector integrates a weighted sum of signals originating in different spectral bands and at different positions in the scene.   In contrast to the FTS and Hadamard-transform spectrometer discussed above, computed-tomography imaging spectrometry involves spectral as well as spatial multiplexing.   To demultiplex the raw data, many weighted sums (as independent as possible) must be collected.   To eliminate scanning, these sums have to be obtained simultaneously.   One method of collecting multiple sums
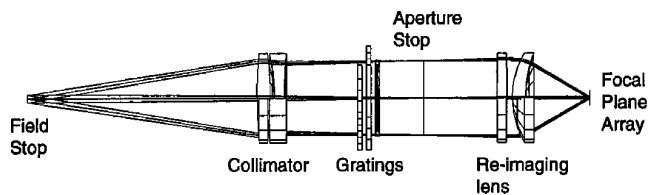
in parallel is to use crossed gratings and a FPA (see Fig. 2).

We assume in Fig. 2 that an objective optic (lens or telescope, not shown) places an image in the field-stop plane.   The field stop itself is a 2D aperture, such as a square.   As noted in the figure, the remaining elements are conventional with the exception of the dispersive stage that consists of three sequentially rotated gratings.   The dispersion directions of the gratings are separated by 60°.   The result is a hexagonally symmetric set of dispersion images as illustrated in Fig. 3.

The border in Fig. 3 indicates the extent of the FPA. Each shaded area represents a dispersed image of the field stop.   Each image arises from a particular combination of diffraction orders at each of the three gratings.   The center square area is a direct (no dispersion) image of the field stop.   Furthermore each dispersed image may be interpreted as a parallel projection of a 3D volume.   We explore this interpretation in more detail below.

The use of crossed gratings to collect information simultaneously can be found in many applications, one example being shearing interferometry in optical testing.[4]   Two crossed gratings within the context of imaging spectrometry were proposed originally and implemented in a working instrument by Okamoto et al.[5]   The optimal number of gratings and more generally the design of the dispersive element for the
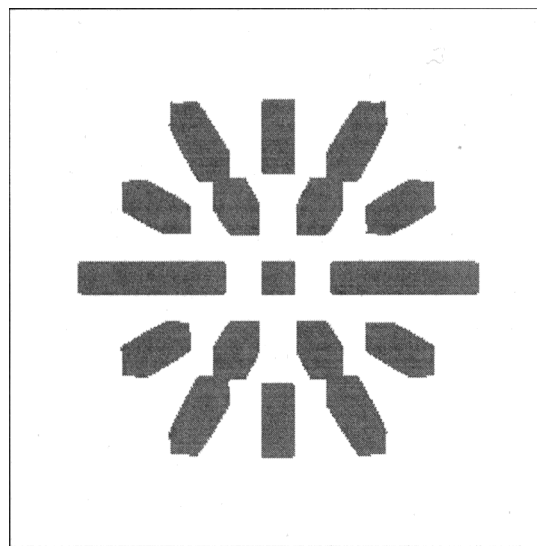

Fig. 3.   Irradiance distribution on the FPA.

computed-tomography imaging spectrometer remain open questions at this point.

Although computed tomography may be best known for its application in the context of medical imaging, its usefulness extends beyond imaging volumes-of-matter. In fact the ideas initially developed by the Austrian mathematician Radon[6] apply to any multidimensional function as long as lower-dimensional integrals of this function can somehow be formed. In the case of imaging spectrometry the multidimensional function is the 3D (x, y, λ) object cube. This interpretation has been used in several cases. Systems based on computed-tomography concepts and using gratings,[5,7] multiple prisms,[8] rotating prisms,[9] and a rotating instrument[10] have all been recently proposed. The advantage of the design presented here is that it makes possible snapshot imaging spectrometry by collecting all data necessary for reconstruction of the object cube in one image.

3. Theory

The dispersed images of the radiance distribution within the field stop (Fig. 3) may be interpreted as parallel projections of a continuous 3D volume onto a plane. Figure 4 illustrates that interpretation for a discrete set of azimuth angles and the same projection angle. Projection angles are measured from the λ axis. The maximum projection angle shown in the figure is therefore $\sim 45°$. The circled numbers indicate diffraction orders. The boxed letters associate the orders with one of the three gratings present in the imaging spectrometer.

According to the central-slice theorem,[11] the 2D Fourier transform of each projection equals a plane through the 3D-frequency-space (ξ, η, l) representation of the object cube. Each plane contains the
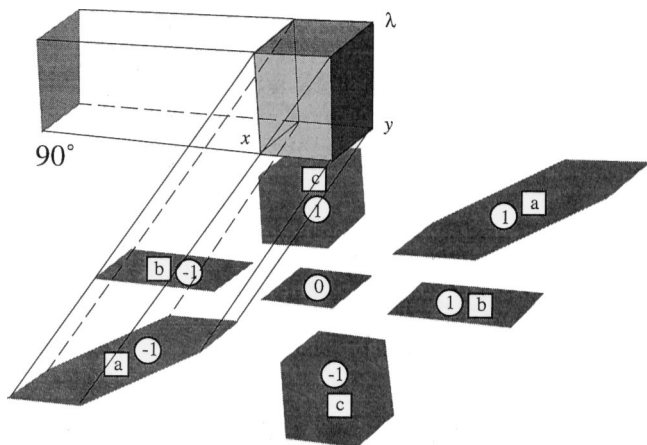

Fig. 4. Diffracted images of the field stop as parallel projections of a 3D object. The projection angle is defined as measured from the λ axis in this illustration. The projection marked 0 therefore corresponds to 0°, whereas the ±1 projections are taken at azimuth angles incremented by 60° and a projection angle of $\sim 45°$. See text for a discussion of the projection marked 90°. The center image plays a double role. In addition to being a valid projection it is also a direct image of the field stop forming a polychromatic image of the viewed scene.

origin, and each plane's normal is oriented at the same azimuth and projection angle as the direction of projection. A 3D-frequency-space representation of the projections in Fig. 4 is shown in Fig. 5.

The central-slice theorem indicates that 2D projections contain information sufficient to reconstruct a general object cube. The objective is to collect enough projections to determine the 3D-frequency-space representation of the object cube fully. The 3D real-space (x, y, λ) distribution of the object cube is then recovered through an inverse 3D Fourier transform. Recovery of a 3D distribution from 2D projections is known as the x-ray transform.[12] In general the exact procedure for collecting frequency-space data depends on the specifics of the imaging system.[13] One possible scheme is to obtain 2D projections at a projection angle of 90° (see Fig. 4) and a continuous range of azimuth angles from 0° to 180°. According to the central-slice theorem, this amounts to sweeping out 3D frequency space by means of a plane whose normal lies in the $\xi\eta$ plane and that rotates about the l axis. In practice the requirement for a continuum of projection data is relaxed, and satisfactory results may be obtained with a finite number of projection angles.[11]

The central-slice theorem also reveals an important limitation of the computed-tomography imaging spectrometer. This limitation is imposed by the finite area of the FPA and the diffraction efficiency decreasing at higher diffraction orders. These two factors combine to impose an upper bound on the projection angle. Projections cannot be recorded at angles ranging from the upper-bound projection angle to as high as 90° (Fig. 4). In 3D frequency space the complement of the upper-bound projection angle defines the half-angle extent of two missing cones with vertices at the origin.[14] (A cutaway view of 3D frequency space and the missing cones is shown in Fig. 6.) Consequently we cannot fully determine the 3D-frequency-space distribution of the object cube. Figure 6 also assumes a continuous range of azimuth angles at which projections are collected. This is itself an idealized situation. As illustrated in Fig. 3, we have access only to discrete azimuth angles. The projec-
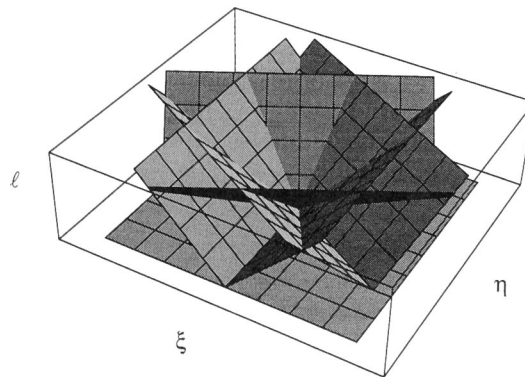

Fig. 5. Three-dimensional, frequency-space interpretation of Fig. 4. Only the upper half-space, $l \geq 0$, is shown. Each plane corresponds to a unique projection and azimuth angle pair in Fig. 4.

tion data as shown in Fig. 3 yield a set of discrete planes within the filled volume in Fig. 6.

A unique reconstruction of the object cube is therefore impossible. In practice, however, the missing-cones deficiency in the collected data may be countered through the use of constraints on the reconstruction process. These constraints express any *a priori* knowledge of the object cube. A simple example is the positivity constraint requiring the reconstructed object cube to be non-negative. Each atmospheric spectral window may also offer its own set of constraints (prominent absorption lines, for example). The chosen constraints work to fill the missing cones indirectly.

Object cubes whose 3D-frequency-space representations lie inside the missing cones pose the greatest challenge to the reconstruction effort. Such difficult object cubes contain little spatial structure (flat-field illumination of the entire field stop, for example) and sharp spectral emission (or absorption) features. Note also a related and interesting consequence of the missing cones. The spectral resolution of the imaging spectrometer depends on the spatial size of features within the field stop. Finer features can be reconstructed at a higher spectral resolution.

A. Discrete-to-Discrete Model Formalism

The central-slice theorem and the x-ray transform provide the means to interpret at least qualitatively the projection data collected by the nonscanning imaging spectrometer. As a result of this interpretation, we have already identified the limitations posed by the finite FPA area and low diffraction efficiency at higher diffraction orders.

Intuitively, more projections should lead to better reconstruction results. The central-slice theorem identifies what projection data are needed to characterize fully the 3D-frequency-space representation of the object cube. Ideally the optical system should

provide views of the object cube at various azimuth angles and a projection angle of 90° (see the projection geometry in Fig. 4). The central-slice theorem can guide the design of the imaging spectrometer's optics and diffractive elements.

The x-ray-transform algorithm, however, is not well suited to object-cube reconstruction in the case of the imaging spectrometer described here. The algorithm is based on several unrealistic assumptions: The image-detecting medium is continuous, and the imaging system is free of diffraction effects and image-quality-degrading aberrations, the measured data are not corrupted by noise, and projection data can be obtained at any azimuth and projection angle.[15] Our imaging spectrometer violates all three assumptions. The image-detecting medium is an array of finite-area, discrete detector elements. The projection data collected by the FPA are corrupted at least by quantum noise. Finally, as shown in Fig. 3, projections are available only at a discrete set of azimuth and projection angles.

We need to define a more realistic model of the imaging spectrometer. The model must account for the finite number of discrete measurements collected by the FPA. The model must also account for the fact that reconstruction takes place on a digital computer. The reconstruction result is therefore in the form of a finite, discrete set of numbers. Consequently the object cube needs to be described by discrete numbers to be compatible with both the measurement data and digital-reconstruction algorithms.[15] The result is the discrete-to-discrete model of the computed-tomography imaging spectrometer. The imaging spectrometer maps a discrete object cube to a discrete set of measurements.

A common method of discretizing a continuous object cube is by averaging it over small-volume elements (voxels, see Fig. 7). If N voxels are used to cover the 3D (x, y, λ) extent of the object cube, the object cube can be expressed through N numbers denoted f_n, $n = 1, \ldots, N$. Furthermore these num-
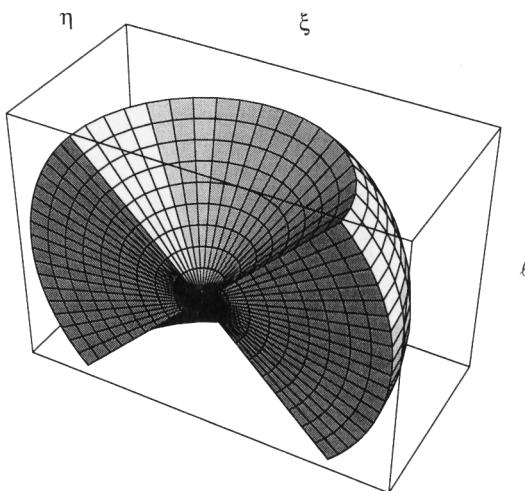

Fig. 6. Missing cones in 3D frequency space. For clarity only a half-space is shown. The half-angle of the missing cones is the complement of the maximum projection angle achievable with the imaging spectrometer.
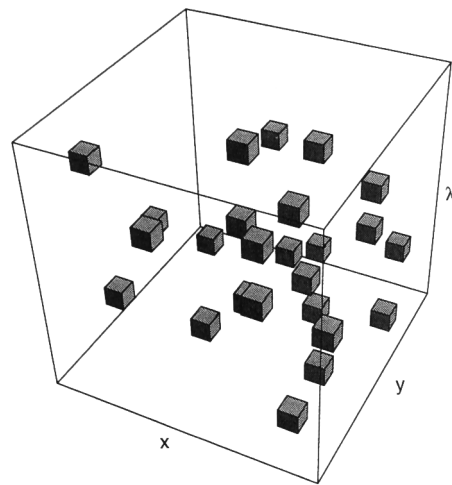

Fig. 7. Voxel representation. The full set of voxels fills the entire object cube.

bers can be arranged to form a vector **f**. Note that the vector **f** is an approximation of the object cube: Features smaller than a voxel are lost in the averaging process.

We denote the finite set of measurements derived from the FPA by g_m, $m = 1, \ldots, M$, where M is the number of detector elements. The measurement data can also be arranged into vector form, resulting in the data vector **g**.

The effect of the imaging system is described by means of a $M \times N$ system matrix $\mathscr{H}$, which operates on the object-cube vector **f** and produces the M-element vector **g**, representing the output image. More succinctly,

$$\mathbf{g} = \mathscr{H}\mathbf{f} + \mathbf{n}, \tag{1}$$

where **n** (also an M-element vector) represents additive system noise. Equation (1) surfaces often in image reconstruction applications and in the case of spectrometry may be used quite generally to describe any type of instrument.

Each column of $\mathscr{H}$ contains the imaging spectrometer's response to a small pointlike source, i.e., a voxel. To calibrate the spectrometer by determining $\mathscr{H}$, this pointlike source is translated to positions on a rectangular 3D lattice, specified by $(\bar{x}, \bar{y}, \bar{\lambda})_n$, $n = 1, \ldots, N$. The bars associate the coordinates with the lattice. If every column of $\mathscr{H}$ is normalized by the corresponding voxel's radiance, each element H_{mn} is the joint probability $\Pr(m, n)$ that a signal originating in the nth voxel will be detected by the mth detector element.

The formalism of Eq. (1) allows for calibration of the computed-tomography imaging spectrometer in terms of basis functions other than voxels. Voxels are fundamental in the sense that each is localized, and so relationships between radiance values at different positions in the object cube are not expressible. Voxels are also a convenient choice of basis from an experimental viewpoint.

4. Experimental Implementation

Every detector element has the potential to contribute additional information about the object cube, barring an overlap of projections. It is therefore to our benefit to cover as much of the FPA as possible with nonoverlapping projections. We determined that three gratings, rotated sequentially by 60°, provided an efficient packing of different azimuth and elevation angle projections in the case of a rectangular FPA (see Fig. 3). We did not use more gratings for two reasons: Instrument transmittance would have suffered, and the FPA was already well filled with projection data.

Thirteen sinusoidal phase gratings were produced interferometrically with silver-halide plates with varying zero-to-peak phase delays (see Fig. 8). The zero-to-peak phase delay of a sinusoidal phase grating determines that grating's diffraction efficiencies into all orders.[16] Figure 8 is based on diffraction efficiencies measured at 632.8 nm. The continuous line and
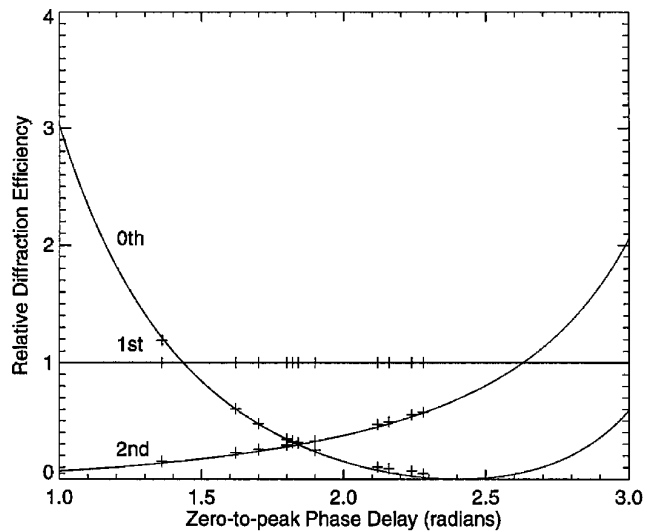

Fig. 8. Graphic representation of the produced gratings. The gratings' efficiencies were measured at 632.8 nm and are denoted by plusses. The continuous curves and line represent the theoretical variations of efficiency with zero-to-peak phase delay for different orders (0th, 1st, and 2nd). All theoretical and measured diffraction efficiencies have been related to the ±1st diffraction-order efficiency.

curves marked 0th, 1st, and 2nd in the figure are the theoretical diffraction-efficiency curves.[16] All theoretical and measured diffraction efficiencies in Fig. 8 are related to the ±1st diffraction-order efficiency. This way the theoretical and experimental diffraction efficiencies may be compared without knowledge of the order-independent transmittance associated with each experimental grating.

The grating constant was set at 14 μm. This choice was dictated by our intent to capture on the FPA diffraction orders to the third order at the long-wavelength end of the spectrometer's bandwidth. The area of the FPA and the focal length of the reimaging lens then determined the grating constant (Table 1).

In selecting the optimal set of three gratings, the dynamic range of the detector array had to be considered. The objective was to maintain approximately the same irradiance level at all projections. An accurate analysis must account for the fact that a

Table 1. Imaging Spectrometer Parameters

Parameters	Specifications
Number of gratings	3
Rotation angle between gratings	60°
Grating constant	14 μm
Grating type	Transmission, sinusoidal phase
Collimator focal length	245 mm
Reimaging lens focal length	28 mm
FPA dimensions	8.8 mm (H) × 6.6 mm (V)
Imaging-spectrometer bandwidth	470–770 nm

detector element may integrate spectral irradiance over a wider (low-dispersion) or narrower (high-dispersion) bandwidth. An additional complication appears in the case of three gratings rotated at 60° increments. There are several sequences of diffraction orders that lead to the same point on the FPA. This degeneracy means that minimizing the transmittance for a particular order sequence may not minimize the irradiance on a given section of the FPA because of high transmittance in other order sequences that lead to the same region of the array.

Given 13 gratings taken three at a time, there were 1716 combinations to be evaluated. We did not perform a polychromatic analysis and only accounted for the degeneracy in diffraction-order sequences. The grating set that was chosen produced a maximum-entropy distribution of monochromatic (632.8-nm) irradiance levels. The entropy was calculated through

$$H = -\sum_{i=1}^{K} \tau_i \ln \tau_i,$$

where K is the number of projections on the FPA and τ_i represents the ith projection's share of the total irradiance.

The chosen gratings have approximately the same zero-to-peak phase delay and are characterized by peak diffraction efficiency in the first order (zero-to-peak phase delay of ~1.83 rad at 632.8 nm). We have not yet attempted a direct inversion leading from the desired uniform irradiance levels to the corresponding grating set. Figure 9 shows the experimental polychromatic performance of the maximum-entropy set. Note that the center image remains much brighter than its dispersed brethren despite the fact that the zeroth-order diffraction efficiency for each grating remains low. The high irradiance is due to cancellation of high-efficiency diffraction orders leading back to the center of the array.

The spectral response of our FPA ranges from 400 to 1100 nm. Because the calibration of the spectrometer is done with a grating monochromator, the operating bandwidth of the instrument must be limited to less than one octave (400–800 nm) to prevent overlapping projections from being detected. An effective way to trim the FPA's responsivity is by means of a hot-mirror filter (see Table 1 for passband limits).

Minification of the field stop by lengthening the focal length of the collimator lens effectively increases the dispersion available within the system at the expense of spatial resolution.[17] We are thus presented with a trade-off between spatial resolution and reducing the half-angle of the missing cones. We implemented an approximately tenfold minification with our choices of collimator-lens and reimaging lens focal lengths (Table 1 and Fig. 10).

Finally, the reimaging lens must have a very good field performance to accommodate field angles from higher diffraction orders. We found that a commercial photographic lens was well suited to this task because the size of a 35-mm film frame is well in excess of our FPA's area (Table 1).

5. Experimental Calibration

It is possible in principle to model the output of the imaging spectrometer analytically and thus calculate the mapping matrix $\mathcal{H}$. The model approach requires detailed knowledge of the optics and associated aberrations, system alignment, properties of the dispersive elements, and the detecting medium. An IR FPA, for example, may be plagued by detector-to-detector responsivity nonuniformity. Any effects not accounted for in a theoretical model will cause the model-based $\mathcal{H}$ to describe an imaging spectrometer that is different from the one collecting the projection data. Such an inconsistency will adversely affect the reconstruction effort and introduce errors into the estimate of the object cube, denoted by $\hat{\mathbf{f}}$. The solution is to determine $\mathcal{H}$ experimentally. The
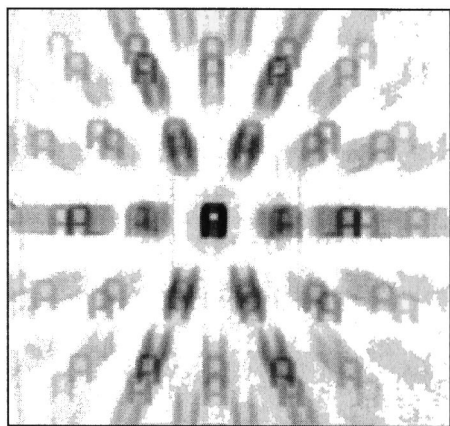

Fig. 9. System image of the U (green phosphor) and A (red phosphor) test target. Note that the dispersed images (i.e., object-cube projections) are collected only at a discrete set of polar coordinates.
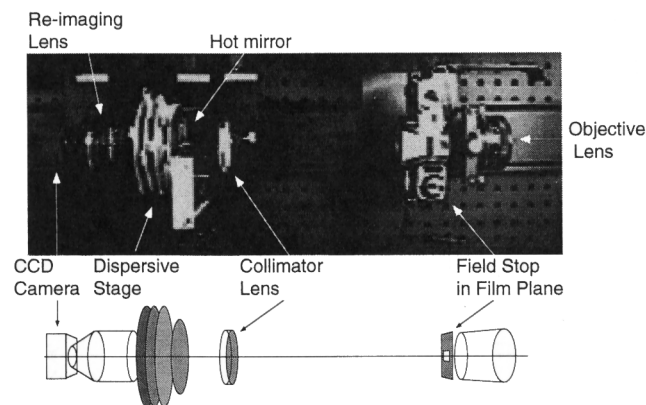

Fig. 10. Layout of the instrument in an operational configuration. The lower diagram provides a road map of the various components. The presence of the camera body allows us to install lenses of different focal lengths easily, changing field-stop image magnification.

experimental-calibration approach already has a direct analog in medical-imaging applications.[18]

In practical terms, the algorithm is as follows. A set of basis functions is chosen with which **f** is discretized. Next the response of the instrument to each basis function is measured and subsequently forms a column of $\mathscr{H}$. Depending on the resources available, we can record the responses either to every basis function or to just a subset and interpolate the remainder.

The matrix $\mathscr{H}$ needs to be determined only once. Subsequent operation of the imaging spectrometer requires only a relatively fast inversion of this matrix. The instrument should be adjusted occasionally to account for changes in its constitution, such as misalignment of the optics.

We chose to work with voxels as basis functions (see Fig. 7). The spatial extent of each voxel was determined by the dimensions of an image of a light-guide fiber face. The spectral dimension was controlled by the operating parameters of a grating monochromator. The resulting voxel dimensions were $\Delta x = \Delta y = 0.45$ mm and $\Delta\lambda = 15$ nm. The field stop was a 5 mm $\times$ 5 mm aperture. The lattice of positions that the fiber-face image explored was 11×11 spatial positions by 20 spectral bands ($N = 2420$). For any given voxel, the image of the fiber face was translated to the correct $(\bar{x}, \bar{y})$ coordinates within the field stop, and the monochromator selected the appropriate central wavelength, $\bar{\lambda}$. The output image was recorded by a CCD camera and a frame grabber (see Fig. 11). Either the monochromator, the fiber-face image, or both were then translated to the next $(\bar{x}, \bar{y}, \bar{\lambda})$, and the process was repeated until all voxels had been calibrated. Each voxel's image through the imaging spectrometer was then used to form a column of $\mathscr{H}$.

Many cameras that operate in the visible spectrum have the option of gamma correction, resulting in the output video voltage being related to input irradiance through $V_{\text{out}} = KE^\gamma$. The parameter γ is supposed to correct for the nonlinear transfer function of a display video monitor. The result of such correction is that the spatial-radiance distribution of the image displayed is linearly proportional to the radiance of the imaged scene. In the case of our camera, γ may be set to values $0.45 \leq \gamma \leq 1$.

Any value of γ other than unity results necessarily in a nonlinear camera response. For our purposes the video output is not being sent to a TV monitor but rather to a frame grabber. The resulting nonlinearity must be eliminated because one of the tenets of our approach is that the imaging spectrometer is a linear system. In principle, γ could be set to one. In practice, we opted for a setting that satisfied certain dynamic range considerations and then measured the camera transfer function directly. Any data collected later had to be corrected by means of the inverse of this transfer function (through a look-up table) before being used in reconstruction algorithms.

6. Reconstruction Algorithm and Results

A reconstruction algorithm may be optimized to take full advantage of properties unique to the (x, y, λ) object cube. The optimization may take the form of appropriate constraints applied at each iteration of the algorithm. For now, however, we chose to abstain from such an effort and used the expectation–maximization algorithm[19] with no explicit constraints. The algorithm's aim is to maximize the likelihood $\Pr(\mathbf{g}|\mathbf{f})$.[20] We assume that the likelihood is a Poisson distribution (the detector output is photon noise limited) and that all elements of the data vector **g** are independent.

The initial guess at the object (denoted by the superscript in parentheses) was generated through backprojection of the measurement vector onto the object space:

$$\hat{f}^{(0)} = \mathscr{H}^T \mathbf{g}. \tag{2}$$

The expectation step computes the vector $\hat{g}$ based on the current $\hat{\mathbf{f}}$ through Eq. (1) with $\mathbf{n} \cong 0$. The subsequent maximization step computes a correction factor for every element of our object estimate. Formally,

$$\hat{f}_n^{(k+1)} = \frac{\hat{f}_n^{(k)}}{\displaystyle\sum_{m'=1}^{M} H_{m'n}} \sum_{m=1}^{M} H_{mn} \frac{g_m}{\hat{g}_m^{(k)}}, \tag{3}$$

where the letters in italics denote matrix or vector elements. The algorithm stops when the quotients in the summands go to unity and therefore $\hat{\mathbf{f}} = \hat{\mathbf{f}}_{\text{max.likelihood}}$. No positivity constraint is needed, because, given a non-negative initial guess, the multiplicative nature of Eq. (3) guarantees that all further estimates will be greater than zero.

A check on the performance of the algorithm was accomplished with one of the voxel calibration images (Fig. 11) as the measurement vector **g**. Because this
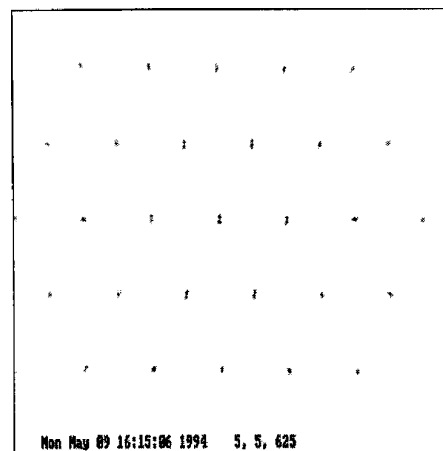

Fig. 11. Typical calibration image. The matrix $\mathscr{H}$ is constructed from these kinds of data. Each image forms one column of the matrix. Certain sequences of diffraction orders cancel imperfectly and cause the double-dot images of the input voxel.

image forms a column in $\mathcal{H}$, the estimate $\hat{\mathbf{f}}$ should be of the form $[0, 0, \ldots, 0, s, 0, \ldots, 0, 0]^T$ with the position of the nonzero element s corresponding to the column formed by the said voxel image. Having confirmed this result, we moved to more ambitious targets.

Finally, a given detector element's field of view within the object cube may be determined by means of Eq. (2) with $\mathbf{g} = [0, 0, \ldots, 0, 1, 0, \ldots, 0, 0]^T$. This time the position of the unity element corresponds to the detector of interest. The resulting vector $\mathbf{f}$ will contain nonzero values only at those voxels that are seen by the detector element.

A. Target Generation

A TV color monitor is a very flexible target generator. A spatial pattern can easily be produced and fed into the output buffer on the frame-grabber board. This image is then displayed on the monitor with red, green, or blue phosphor or a combination of the three phosphors. Because each of the primary phosphors composing the screen has a different spectral energy distribution, we can generate a broad range of target object cubes. The fact that the blue and green phosphors are band emitters, whereas the red is a line emitter, makes the TV monitor even more useful.[21] Alternatively, a monitor may also be combined with a TV color pattern generator to generate spatial and spectral targets.

B. Reconstruction Results

We generated a University of Arizona target consisting of the letter U displayed on the green phosphor and the letter A displayed on the red phosphor. The image recorded on the CCD is shown in Fig. 9 and was used to form the data vector $\mathbf{g}$. Figure 12 shows the sequence of 20 spectral images that constitute $\hat{\mathbf{f}}$ following 30 iterations with Eq. (3). The format of

Fig. 13. Comparison of measured and reconstructed spectra. The broad gray curve represents the spectral emission of the monitor measured directly with a spectrometer. The thin, black curves represent the reconstructed estimates of the same spectral emission. Each of the two estimated spectra comes from a location on the target common to both the letter U and the letter A.

each image is 11×11 pixels. Convergence was judged based on the decrease in the Euclidean norm of the residual $\| \mathbf{g} - \mathcal{H}\hat{\mathbf{f}} \|$ after each iteration.

In Fig. 13 we compare the reconstruction results along the spectral dimension of the object cube with direct measurements of the monitor output taken with a spectrometer and a radiometer. The broad, gray curve represents the direct measurements. The width of the gray curve at a particular wavelength is the uncertainty in that measurement of the monitor's spectral radiance. The continuous black curves represent the results of the object-cube reconstruction. The two reconstructed spectra are taken
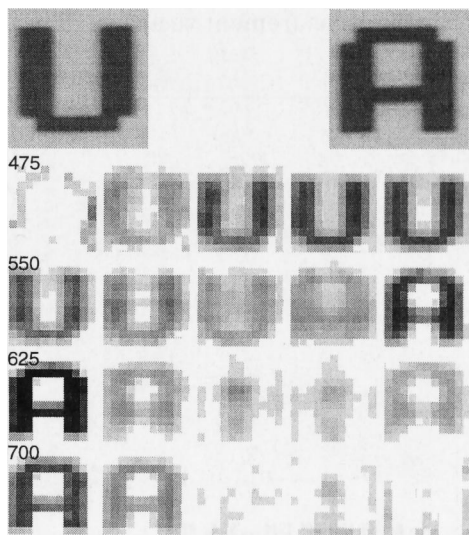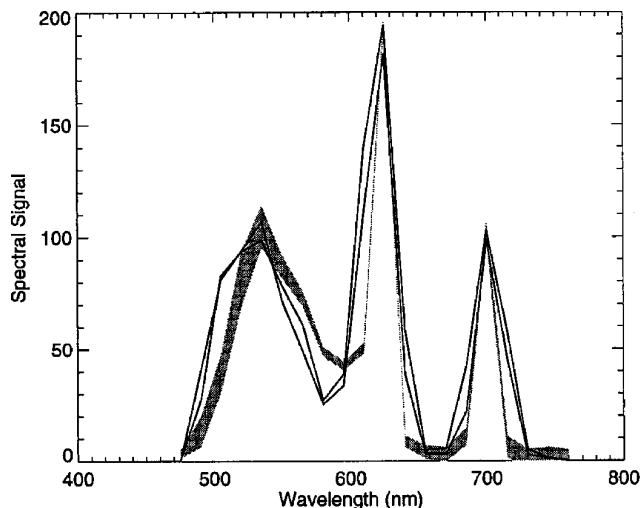

Fig. 12. University of Arizona U and A phantoms and object-cube reconstruction results. Our test target consisted of two letters, each displayed on a different phosphor (top part of figure). The U was shown in green, and the A was shown in red.
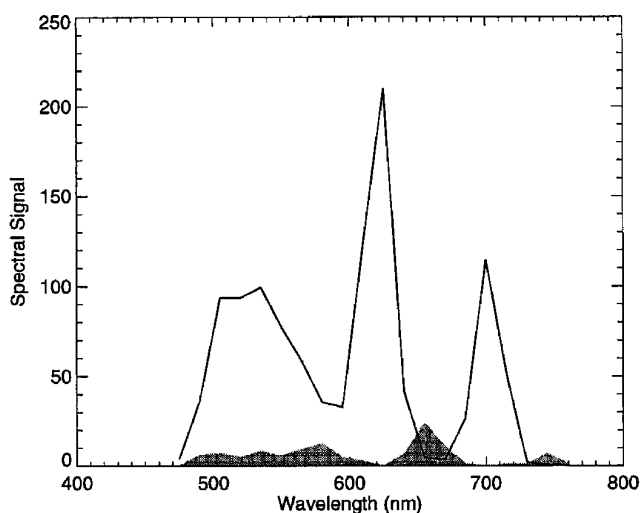

Fig. 14. Background signal versus the spectral signature. The background signal (shown in gray) is associated with a nonemitting part of the target. The black curve indicates the spectrum found at a part of the target common to U and A.

from target spatial locations common to both the letter U and the letter A.

In Fig. 14 we compare the reconstructed spectrum from an emitting location on the target to the spectrum from a location in a nonemitting part of the target (shown in gray). The latter spectrum represents a background signal introduced in the reconstruction process.

7. Discussion and Conclusions

We have presented a design for a visible-spectrum (470–770-nm), temporally and spatially nonscanning, computed-tomography imaging spectrometer. Elimination of scanning carries two advantages. First, the spectrometer no longer requires moving elements; therefore it is more rugged. Second, a nonscanning spectrometer can record dynamic events in object space.

The most essential element of this imaging-spectrometer design is the dispersive stage. The stage consists of three transmission sinusoidal-phase gratings, rotated with respect to one another at increments of 60°. These gratings disperse the radiance contained within the field stop of the imaging spectrometer (Fig. 10) in multiple directions and into multiple diffraction orders (Fig. 9). Each dispersed image of the field stop can be interpreted as a parallel projection of a 3D (x, y, λ) object cube (see Fig. 4).

The projections were interpreted with the central-slice theorem. The theorem relates the projection data to slices through the 3D (ξ, η, l) frequency-space representation of the object cube. Use of the frequency-domain viewpoint revealed that the finite area of the FPA and decaying diffraction efficiency at higher diffraction orders lead to two missing cones centered on the l axis in frequency space (Fig. 6). The imaging spectrometer presented in this paper is an example of a limited-view-angle tomographic system. Scenes containing extended sources with little spatial structure and sharp spectral emission (or absorption) features will be most difficult to reconstruct. Consider as examples imaging clouds or the blue sky.

The objective of reducing the half-angle of the missing cones is equivalent to obtaining higher-dispersion images of the field stop. We propose three approaches. First, lengthening the collimator-lens focal length while keeping all other system parameters fixed can reduce the extent of the missing cones at the expense of the spatial resolution. In the limit, minification of the field-stop image leads to a pinhole-entrance-aperture spectrometer with no spatial resolution. Second, the dispersive element(s) need to uniformly distribute the polychromatic irradiance incident on the FPA among all the detected projections. A high signal-to-noise ratio is especially important at the high-diffraction-order images of the field stop. These images are the ones that come closest to the desired side view of the object cube, marked 90° in Fig. 4. Third, a larger-format FPA than the one used in our system (Table 1) can collect images of the field stop at higher diffraction orders.

An additional consequence of the central-slice theorem is the notion that the imaging spectrometer's spectral resolution depends on the spatial size of features in the scene; the finer the features, the better the spectral resolution. We hereby suggest that the central-slice theorem is a useful tool in the evaluation of competing computed-tomography, imaging-spectrometer designs.

The experimental implementation of the instrument relied on the discrete-to-discrete model of the imaging spectrometer. To fit into the digital framework imposed by discrete data and digital-reconstruction algorithms, the continuous object cube had to be discretized. We approximated the object cube, using 2420 voxels.

The matrix operator $\mathscr{H}$, which maps the object cube **f** to measurement data **g**, was characterized experimentally. A small, pointlike source was translated on a 3D $(\bar{x}, \bar{y}, \bar{\lambda})$ rectangular lattice and the imaging spectrometer's response (effectively the point spread function) was recorded at each lattice position. Such direct characterization assured us of an accurate description of the system.

Using a color TV monitor and taking advantage of the differing spectral-energy distributions of the phosphors, we generated a simple University of Arizona target consisting of the letters U and A. The imaging spectrometer had been previously calibrated on a 11 $\times$ 11 $\times$ 20 voxel lattice. The lattice dimensions refer to the number of positions along the two spatial dimensions and the spectral dimension of the object cube, respectively. Reconstruction of the object cube from the measurement data **g** was performed with the expectation–maximization algorithm without any explicit constraints. Results indicate a good performance in the case of the broadband-emitting green phosphor and the line-emitting red phosphor (Figs. 12 and 13).

The encouraging aspect of this type of imaging spectrometer is its potential for increased spatial and spectral resolution. Further developments in staring-FPA and computing technologies, improved optical and dispersive-element design, and algorithm optimization offer opportunities thus far unexplored.

References

1. G. Vane and A. F. H. Goetz, "Terrestrial imaging spectroscopy," Remote Sensing Environ. **24,** 1–29 (1988).
2. W. Blyleven, DALSA CCD Image Sensors Inc. Waterloo, Ontario, Canada N2V 2E9 (personal communication, 1994).
3. N. J. A. Sloane, T. Fine, P. G. Phillips, and M. Harwit, "Codes for multiplex spectrometry," Appl. Opt. **8,** 2103–2106 (1969).
4. J. C. Wyant, "Double frequency grating lateral shear interferometer," Appl. Opt. **12,** 2057–2060 (1973).

5. T. Okamoto, A. Takahashi, and I. Yamaguchi, "Simultaneous acquisition of spectral and spatial intensity distribution," Appl. Spectrosc. **47,** 1198–1202 (1993).

6. J. Radon, "Über die Bestimmung von Funktionen durch ihre Integralwerte längs gewisser Mannigfaltigkeiten," in *Gesammelte Abhandlungen/Collected Works* (Birkhäuser Verlag, Vienna, 1987), Vol. 2, pp. 11–26.

7. T. Okamoto, and I. Yamaguchi, "Simultaneous acquisition of spectral image information," Opt. Lett. **16,** 1277–1279 (1991).

8. F. V. Bulygin, G. N. Vishnyakov, G. G. Levin, and D. V. Karpukhin, "Spectrotomography—a new method of obtaining spectrograms of 2-D objects," Opt. Spectrosc. (USSR) **71,** 561–563 (1991).

9. J. M. Mooney, "Spectral imaging via computed tomography," in *Proceedings of Infrared Information Symposia (IRIS) Specialty Group on Passive Sensors* [Environmental Research Institute of Michigan (ERIM), Ann Arbor, Mich., 1994], Vol. 1, pp. 203–215.

10. Y. Bétrémieux, T. A. Cook, D. M. Cotton, and S. Chakrabarti, "SPINR: two-dimensional spectral imaging through tomographic reconstruction," Opt. Eng. **32,** 3133–3138 (1993).

11. H. H. Barrett and W. Swindell, *Radiological Imaging/The Theory of Image Formation, Detection, and Processing* (Academic, New York, 1981), Vol. 2.

12. J. N. Aarsvold, "Multiple-pinhole transaxial tomography: a model and analysis," Ph.D. dissertation (University of Arizona, Tucson, Ariz., 1993), Chap. 2.

13. M. Y. Chiu, H. H. Barrett, R. G. Simpson, C. Chou, J. W. Arendt, and G. R. Rindi, "Three-dimensional radiographic imaging with a restricted view angle," J. Opt. Soc. Am. **69,** 1323–1333 (1979).

14. H. H. Barrett, "Editorial: limited-angle tomography for the nineties," J. Nucl. Med. **31,** 1688–1692 (1990).

15. H. H. Barrett, "Image reconstruction and the solution of inverse problems in medical imaging," in *The Formation, Handling, and Evaluation of Medical Images,* A. Todd-Pokropek and M. A. Viergever, eds. (Springer-Verlag, Berlin, 1991), pp. 3–42.

16. J. Goodman, *Introduction to Fourier Optics* (McGraw-Hill, New York, 1968), Chap. 4, pp. 69– 70.

17. M. R. Descour, "Non-scanning imaging spectrometry," Ph.D. dissertation (University of Arizona, Tucson, Ariz., 1994), Chap. 2.

18. R. K. Rowe, "A system for three-dimensional SPECT without motion," Ph.D. dissertation (University of Arizona, Tucson, Ariz., 1991), Chap. 5.

19. L. A. Shepp and Y. Vardi, "Maximum likelihood reconstruction for emission tomography," IEEE Trans. Med. Imaging **MI-1,** 113–122 (1982).

20. B. R. Frieden, *Probability, Statistical Optics, and Data Testing* (Springer-Verlag, Berlin, 1991), Chap. 17.

21. D. L. Say, R. A. Hedler, L. L. Maninger, R. A. Momberger, and J. D. Robbins, "Monochrome and color image-display devices," in *Television Engineering Handbook,* K. B. Benson, ed. (McGraw-Hill, New York, 1992), Chap. 12.